

Are nuclear matter properties correlated to neutron star observables ?

Jin-Biao Wei¹, Jia-Jing Lu^{1,2}, G. F. Burgio¹, Zeng-Hua Li², and H.-J. Schulze¹

¹ INFN Sezione di Catania, Dipartimento di Fisica e Astronomia, Università di Catania,
Via S. Sofia 64, I-95123 Catania, Italy

² Institute of Modern Physics, Key Laboratory of Nuclear Physics and Ion-beam Application (MOE), Fudan University,
Shanghai 200433, P.R. China

Received: date / Revised version: date

Abstract. We investigate properties of nuclear matter and examine possible correlations with neutron star observables for a set of microscopic nuclear equations of state derived within the Brueckner-Hartree-Fock formalism employing compatible three-body forces. We find good candidates for a realistic nuclear EOS up to high density and confirm strong correlations between neutron star radius, tidal deformability, and the pressure of metastable matter. No correlations are found with the saturation properties of nuclear matter.

PACS. 21.65.-f, 26.60.-c, 24.10.Cn, 21.65.Cd, 13.75.Cs.

1 Introduction

Neutron star (NS) observations allow us to explore the equation of state (EOS) of nuclear matter [1, 2] at densities well beyond the ones available in terrestrial laboratories. The nature of matter under conditions of extreme density and stability, found only in the NS core, still remains an open question. In particular, the mass and radius of NSs encode unique information on the EOS at supranuclear densities. Currently the masses of several NSs are known with good precision [3–7], but the information on their radii is not very accurate [8–10], being more elusive than NS masses. Particularly, a measurement of the radius with an error of about 1 km could discriminate between soft and stiff EOSs, as discussed in the current literature [11]. For this purpose, present observations of NICER [12–14] could in principle achieve an accuracy of about 2% for the radius, whereas future planned missions like eXTP [15] will allow us to statistically infer their mass and radius to within a few percent. This information can be used to determine the EOS of the matter in the NS interior, and the nature of the forces between fundamental particles under such extreme conditions.

The recent detection by the Advanced LIGO and Virgo collaborations of gravitational waves emitted during the GW170817 NS merger event [16–18] has stimulated an intense research activity towards the understanding of the nuclear matter EOS. In particular, it provided important new insights on the structural properties of these objects, most prominently their masses and radii, by means of the measurement of the tidal deformability [19, 20], and allowed to deduce upper [16, 17] and lower [21] limits on it.

In this paper we compare the constraints on the nuclear EOS obtained from heavy-ion collisions (HICs) with those extracted from the analysis of the NS merger event GW170817. We also examine possible correlations among properties of nuclear matter close to saturation with the observational quantities deduced from GW170817. For this purpose we present recent calculations of NS structure and their tidal deformability using various microscopic EOSs for nuclear configurations.

The paper is organized as follows. In Sec. 2 we give a brief overview of the hadronic EOSs we are using, and in Sec. 3 we discuss their saturation properties at normal nuclear density. Constraints on the NS maximum mass are evaluated and the tidal deformability as important NS observable is introduced in Sec. 4. In Sec. 5 we investigate the compatibility of the EOSs with constraints obtained from HIC data and the GW merger event, and examine possible correlations between both. In Sec. 6 we draw our conclusions.

2 Equations of state

The theoretical description of nuclear matter under extreme density conditions is a very challenging task. Assuming that the most relevant degrees of freedom are nucleons, thus neglecting other particles such as hyperons, kaons, or quarks, the theoretical models can be either microscopic (ab-initio) or phenomenological.

In this paper we use several EOSs based on the microscopic Brueckner-Hartree-Fock (BHF) many-body theory [22, 23], which provides a density expansion [24–26] of

the nuclear-matter binding energy based on the use of realistic two-body forces. It is well known that nucleonic three-body forces (TBF) are needed in order to reproduce correctly the saturation properties of nuclear matter. Currently a complete ab-initio theory of TBF is not available yet, and therefore we adopt either phenomenological or microscopic models [27–30]. The microscopic BHF EOSs employed in this paper, described in detail in Refs. [30, 31], are based on different nucleon-nucleon potentials, namely the Bonn B (BOB) [32, 33], the Nijmegen 93 (N93) [34, 35], and the Argonne V_{18} (V18) [36]. In the latter case, we also provide an EOS obtained with the phenomenological Urbana model for describing TBF (UIX). Useful parametrizations of these EOSs are given in the Appendix.

In the same theoretical framework, we also studied an EOS based on a potential model which includes explicitly the quark-gluon degrees of freedom, named fss2 [42, 43]. This reproduces correctly the saturation point of symmetric matter and the binding energy of few-nucleon systems without the need of introducing TBF. In the following those EOSs are labeled FSS2CC and FSS2GC, indicating two different prescriptions of solving the BHF equations.

We compare these BHF EOSs with the often-used results of the Dirac-BHF method (DBHF) [44], which employs the Bonn A potential, and the APR EOS [45] based on the variational method and the V_{18} potential. For completeness, we also use the well-known phenomenological LS220 [46] and SFHo [47] EOSs, both based on the relativistic mean-field (RMF) approach for the high-density part.

The BHF method provides EOSs for homogeneous nuclear matter, $\rho > \rho_t \approx 0.08 \text{ fm}^{-3}$. For the low-density inhomogeneous crustal part we adopt the well-known Negele-Vautherin EOS [48] for the inner crust in the medium-density regime ($0.001 \text{ fm}^{-3} < \rho \lesssim 0.08 \text{ fm}^{-3}$), and the ones by Baym-Pethick-Sutherland [49] and Feynman-Metropolis-Teller [50] for the outer crust ($\rho < 0.001 \text{ fm}^{-3}$). The transition density ρ_t is adjusted to provide a smooth transition of pressure and energy density between both branches of the metastable EOS. The NS-mass domain that we are interested in, is hardly affected by the structure of this low-density transition region and the crustal EOS [51]: The choice of the crust model can influence the predictions of radius and related deformability to a small extent, of the order of 1% for $R_{1.4}$ [51–53], which is negligible for our purpose. Even neglecting the crust completely, NS radius and deformability do not change dramatically [54].

3 EOS properties at saturation

It is very important that any property of the adopted EOS can be tested at the saturation density $\rho_0 \approx 0.17 \text{ fm}^{-3}$ of symmetric nuclear matter (SNM) [$N = Z$, being $N(Z)$ the neutron (proton) number], where information from laboratory data on finite nuclei is available. In general, in the vicinity of the saturation point the binding energy per nucleon can be expressed in terms of the density parameter $x \equiv (\rho - \rho_0)/3\rho_0$ and the asymmetry parameter

$\delta \equiv (N - Z)/(N + Z)$ as

$$E(\rho, \delta) = E_{\text{SNM}}(\rho) + E_{\text{sym}}(\rho)\delta^2, \quad (1)$$

$$E_{\text{SNM}}(\rho) = E_0 + \frac{K_0}{2}x^2, \quad (2)$$

$$E_{\text{sym}}(\rho) = S_0 + Lx + \frac{K_{\text{sym}}}{2}x^2, \quad (3)$$

where K_0 is the incompressibility and $S_0 \equiv E_{\text{sym}}(\rho_0)$ is the symmetry energy coefficient at saturation, and the parameters L and K_{sym} characterize the density dependence of the symmetry energy around saturation. The incompressibility K_0 gives the curvature of $E(\rho)$ at $\rho = \rho_0$, whereas S_0 determines the increase of the energy per nucleon due to a small asymmetry δ . These parameters are defined as

$$K_0 \equiv 9\rho_0^2 \frac{d^2 E_{\text{SNM}}}{d\rho^2}(\rho_0), \quad (4)$$

$$S_0 \equiv \frac{1}{2} \frac{\partial^2 E}{\partial \delta^2}(\rho_0, 0) \approx E_{\text{PNM}}(\rho_0) - E_{\text{SNM}}(\rho_0), \quad (5)$$

$$L \equiv 3\rho_0 \frac{dE_{\text{sym}}}{d\rho}(\rho_0), \quad (6)$$

$$K_{\text{sym}} \equiv 9\rho_0^2 \frac{d^2 E_{\text{sym}}}{d\rho^2}(\rho_0). \quad (7)$$

Properties of the various considered EOSs are listed in Table 1, namely, the value of the saturation density ρ_0 , the binding energy per particle E_0 , the incompressibility K_0 , the symmetry energy S_0 (note that we use the second definition involving the energy of pure neutron matter (PNM) for the values in the table), and its derivative L at ρ_0 . The curvature of the symmetry energy K_{sym} is only loosely known to be in the range of $100 \text{ MeV} \lesssim K_{\text{sym}} \lesssim 100 \text{ MeV}$ [55, 56], and therefore will not be examined in this paper. In Table I we have also included the experimental ranges for the nuclear parameters and the data available so far from astrophysical observations. We notice that all the adopted EOSs agree fairly well with the empirical values. Marginal cases are the slightly too low E_0 and K_0 for V18, too small/large S_0 for LS220/N93, and too low K_0 for UIX and FSS2GC. The L parameter does not exclude any of the EOSs.

4 Neutron star structure and tidal deformability

A very important constraint to be fulfilled by the different EOSs (assuming a purely nucleonic composition of NS matter) is the value of the maximum NS mass, which has to be compatible with the observational data [4–6], in particular the recent lower limit $M_{\text{max}} > 2.14_{-0.09}^{+0.10}$ [7]. In general relativity, the maximum mass is calculated by solving the Tolman-Oppenheimer-Volkoff (TOV) equations for pressure p and enclosed mass m of a static NS

Table 1. Saturation properties and NS observables predicted by the considered EOSs. Experimental nuclear parameters and observational data from different sources are also listed for comparison. See text for details.

EOS	ρ_0 [fm ⁻³]	$-E_0$ [MeV]	K_0 [MeV]	S_0 [MeV]	L [MeV]	M_{\max} [M_\odot]	$\Lambda_{1.4}$	$R_{1.4}$ [km]
BOB	0.170	15.4	238	33.7	70	2.50	570	12.9
V18	0.178	13.9	207	32.3	67	2.36	442	12.3
N93	0.185	16.1	229	36.5	77	2.25	473	12.7
UIX	0.171	14.9	171	33.5	61	1.96	309	11.8
FSS2CC	0.157	16.3	219	31.8	52	1.94	295	11.8
FSS2GC	0.170	15.6	185	31.0	51	2.08	262	11.5
DBHF	0.181	16.2	218	34.4	69	2.31	681	13.1
APR	0.159	15.9	233	33.4	51	2.20	274	11.6
LS220	0.155	15.8	219	27.8	68	2.04	542	12.9
SFHO	0.157	16.2	244	32.8	53	2.06	334	11.9
Exp.	~ 0.14 - 0.17	~ 15 - 16	220-260	28.5-34.9	30-87	$> 2.14_{-0.09}^{+0.10}$	70-580	10.5-13.3
Ref.	[37]	[37]	[38, 39]	[40, 41]	[40, 41]	[7]	[17]	[17]

configuration

$$\frac{dp}{dr} = -\frac{m\varepsilon(1+p/\varepsilon)(1+4\pi r^3 p/m)}{r^2(1-2m/r)}, \quad (8)$$

$$\frac{dm}{dr} = 4\pi r^2 \varepsilon. \quad (9)$$

The only input required is the EOS $\varepsilon(p)$. As shown in Table 1, many EOS models give compatible values of the maximum mass, apart from UIX, FSS2CC, and marginally LS220. We notice that recent analyses of the GW170817 event indicate also an upper limit of the maximum mass of about 2.2 - $2.3 M_\odot$ [57-60], with which several of the microscopic EOSs (V18, N93, DBHF, and APR) would also be compatible.

The tidal deformability λ , or equivalently the tidal Love number k_2 of a NS [61-63], has recently been acknowledged to provide valuable information and constraints on the related EOS. More specifically, the Love number

$$k_2 = \frac{3}{2} \frac{\lambda}{R^5} = \frac{3}{2} \beta^5 \Lambda = \frac{8}{5} \frac{\beta^5 z}{F}, \quad (10)$$

$$z \equiv (1-2\beta)^2 [2-y_R + 2\beta(y_R-1)],$$

$$F \equiv 6\beta(2-y_R) + 6\beta^2(5y_R-8) + 4\beta^3(13-11y_R) + 4\beta^4(3y_R-2) + 8\beta^5(1+y_R) + 3z \ln(1-2\beta)$$

with $\Lambda \equiv \lambda/M^5$ and $\beta \equiv M/R$ being the compactness, can be obtained by solving the TOV equations (8,9) along with the following first-order differential equation [64],

$$\frac{dy}{dr} = -\frac{y^2}{r} - \frac{y-6}{r-2m} - rQ,$$

$$Q \equiv 4\pi \frac{(5-y)\varepsilon + (9+y)p + (\varepsilon+p)/c_s^2}{1-2m/r} - \left[\frac{2(m+4\pi r^3 p)}{r(r-2m)} \right]^2, \quad (11)$$

with the EOS $\varepsilon(p)$ as input, $c_s^2 = dp/d\varepsilon$ the speed of sound, and boundary conditions given by

$$[p, m, y](r=0) = [p_c, 0, 2], \quad (12)$$

being $y_R \equiv y(R)$, and the mass-radius relation $M(R)$ provided by the condition $p(R) = 0$ for varying p_c .

For an asymmetric binary NS system, $(M, R)_1 + (M, R)_2$, with mass asymmetry $q = M_2/M_1$, and known chirp mass

$$M_c = \frac{(M_1 M_2)^{3/5}}{(M_1 + M_2)^{1/5}}, \quad (13)$$

the average tidal deformability is defined by

$$\tilde{\Lambda} = \frac{16(1+12q)\Lambda_1 + (q+12)\Lambda_2}{13(1+q)^5} \quad (14)$$

with

$$\frac{[M_1, M_2]}{M_c} = \frac{297}{250} (1+q)^{1/5} [q^{-3/5}, q^{2/5}]. \quad (15)$$

From the analysis of the GW170817 event [18], a value of $M_c/M_\odot = 1.186_{-0.001}^{+0.001}$ was obtained, corresponding to $M_1 = M_2 = 1.36 M_\odot$ for a symmetric binary system, $q = 0.73 - 1$ and $\tilde{\Lambda} < 730$ from the phase-shift analysis of the observed signal. A lower limit, $\tilde{\Lambda} > 400$, was deduced from a multimessenger analysis of the GW170817 event combined with an analysis of the UV/optical/infrared counterpart with kilonova models [21]. Recently, this value was updated to $\tilde{\Lambda} \gtrsim 300$ [65, 66], although this lower bound has been disputed [67].

We report in Table 1 the value of the tidal deformability for a $1.4 M_\odot$ NS, and the corresponding radius $R_{1.4}$. It turns out that, requiring both NSs to have the same EOS, leads to constraints $70 < \Lambda_{1.4} < 580$ and $10.5 < R_{1.4} < 13.3$ km [17]. We notice that the values calculated for all the adopted EOSs, and displayed in Table 1, lie in the above intervals with the exception of DBHF.

5 Constraints and Correlations

5.1 Constraints on the symmetry energy

An important test for the EOS has to do with the symmetry energy, for which the experimental constraints are abundant at saturation density (see, e.g., [68–70]). We show in Fig. 1 a set of different experimental constraints together with the values of (S_0, L) predicted by the various theoretical models considered in this paper. More in detail,

- the label “HIC” (blue region) corresponds to the constraints inferred from the study of isospin diffusion in HICs [71];
- the label “Polarizability” (violet region) represents the constraints on the electric dipole polarizability deduced in [72];
- the label “Sn neutron skin” (grey region) indicates the constraints deduced from the analysis of neutron skin thickness in Sn isotopes [73];
- the label “FRDM” (rectangle) corresponds to the values of S_0 and L inferred from finite-range droplet mass model calculations [74];
- the label “IAS + Δr_{np} ” (green diagonal region) indicates the isobaric-analog-state (IAS) phenomenology combined with the skin-width data, and represents simultaneous constraints by Skyrme-Hartree-Fock calculations of the IAS and the ^{208}Pb neutron-skin thickness [75];
- the horizontal band (in red color) labeled “Neutron stars” is obtained from a Bayesian analysis of mass and radius measurements of NSs by considering the 68% confidence values for L [76];
- the dashed curve is the unitary gas bound on symmetry energy parameters derived in Ref. [55]: only values of (S_0, L) to the right of the curve are permitted.

All considered constraints are not simultaneously fulfilled in any area of the parameter space, and this is probably due to the model dependencies that influence the derivation of constraints from the raw data, besides the current uncertainties in the experimental measurements. Given this situation, at the moment no definitive conclusion can be drawn and, except for models predicting values of the symmetry energy parameters outside the limits given in Table 1 (like the LS220 or the N93 EOS), no theoretical models can be ruled out a priori on this basis.

A further crucial point in the understanding of the nuclear symmetry energy is its high-density behavior, which is among the most uncertain properties of dense neutron-rich matter. Its accurate determination has significant consequences in understanding not only the reaction dynamics of heavy-ion reactions, but also many interesting phenomena in astrophysics, such as the explosion mechanism of supernovae and the properties of NSs. In fact several aspects of the NS structure and dynamics depend crucially on the symmetry energy, e.g., the composition and the onset of the direct Urca cooling reaction, which is a threshold process dependent on the proton fraction controlled by the symmetry energy.

A big experimental effort has been devoted during the last few years to constrain the high-density symmetry en-

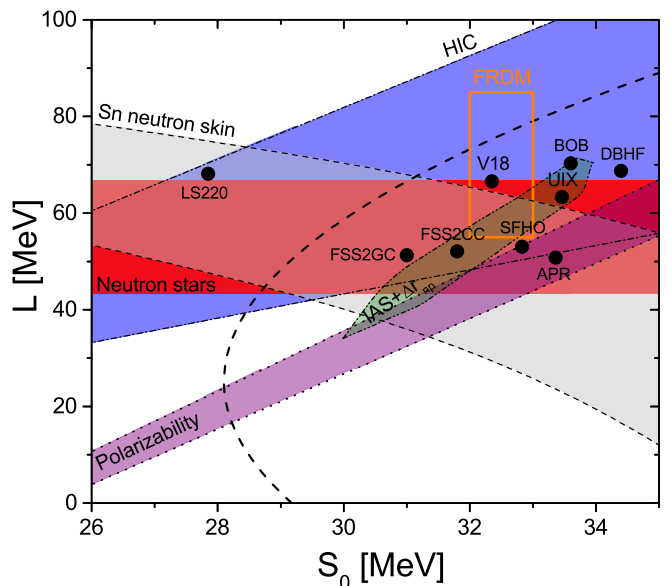


Fig. 1. Correlations between symmetry energy S_0 and its slope L at the saturation density. The markers represent the predictions of the considered EOSs. See text for details on the various constraints.

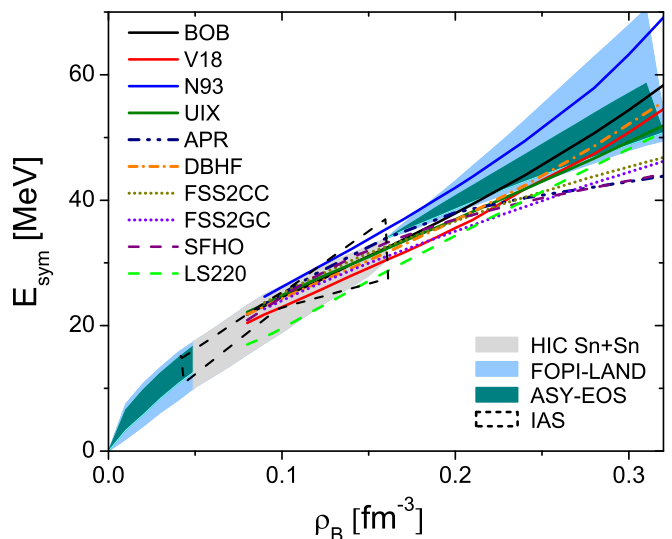


Fig. 2. Symmetry energy vs. baryon density for all considered EOSs. The blue, green, and grey bands, as well as the dashed box, represent experimental data as described in the text.

ergy using various probes in HICs at relativistic energies. Fig. 2 displays some constraints deduced for the density dependence of the symmetry energy from the ASY-EOS data [77] (green band) and the FOPI-LAND result [78] (blue band) as a function of the density. The results of Ref. [71] are reported in the grey area (HIC Sn+Sn), whereas the dashed contour labeled by IAS shows the results of Ref. [75]. We observe that the experimental results exhibit a monotonically increasing behavior with increasing density, and that several microscopic EOSs turn out to be compatible with experiments, except LS220 around saturation density, whereas N93, FSS2CC, and FSS2GC

above the saturation density are only marginally compatible with the data.

5.2 Constraints on the EOS from heavy-ion collisions and gravitational waves

The extraction of the gross properties of the nuclear EOS from HIC data has been one of the main objectives in terrestrial nuclear experiments in the last two decades. In fact HICs at energies ranging from few tens to several hundreds MeV per nucleon produce heavily compressed nuclear matter with subsequent emission of nucleons and fragments of different sizes. The experimental analysis has been performed using the transverse flow as an observable, since it strongly depends on the pressure developed in the interaction zone of the colliding nuclei at the moment of maximum compression. The fireball density reached during the collision can also be probed by subthreshold K^+ production, since this depends on its incompressibility, as shown by the data collected by the KaoS collaboration [80]. A combined flow and kaon production analysis was presented in Ref. [81], where a region in the pressure vs. density plane was identified, through which a compatible EOS should pass.

That analysis is displayed in Fig. 3 (left panels) as a grey box for the flow data by the FOPI collaboration [82], and as a brown box for the KaoS collaboration [80]. Those results point in the direction of a soft EOS, with values of the incompressibility K in the range $180 \leq K \leq 250$ MeV close to the saturation density. We observe that almost all considered EOSs are compatible with the experimental data, except the BOB, V18, and DBHF EOS, which are too stiff at large density, where the analysis could however be less reliable due to the possible appearance of other degrees of freedom besides nucleons. Such densities are actually never reached in HICs. For completeness, we display in the central panels (b) the pressure for the PNM case.

The EOS governs also the dynamics of NS mergers. In fact, the possible scenarios of a prompt or delayed collapse to a black hole or a single NS, following the merger, do depend on the EOS, as well as the amount of ejected matter which undergoes nucleosynthesis of heavy elements. During the inspiral phase, the EOS strongly affects the tidal polarizability Λ , Eq. (10). The first GW170817 analysis for a $1.4 M_\odot$ NS [16] gave an upper limit of $\Lambda_{1.4} < 800$, which was later improved to $\Lambda_{1.4} = 190_{-120}^{+390}$ by assuming that both NSs feature the same EOS [17]. In this new analysis, the values of the pressure as a function of density were extracted, and those are displayed as colored areas in Fig. 3(c), in which the blue (green) shaded region corresponds to the 90% (50%) posterior confidence level. We notice that almost all EOSs turn out to be compatible with the GW170817 data at density $\rho > 2\rho_0$, with BOB in marginal agreement at large density. This constraint combined with the recent observation of the new maximum mass $M = 2.14_{-0.09}^{+0.10} M_\odot$ of PSR J0740+6620 [7] represents at the moment the strongest test for any EOS model. In our case, the V18 EOS appears the most compatible with both data sets. This point has also been dis-

cussed in the framework of phenomenological EOSs [83], where the combined data help to constrain the range of values of the stiffness of isospin-symmetric nuclear matter. A further comparison of HIC data with GW observations can be found in Ref. [84].

Another interesting quantity to consider is the so-called symmetry pressure,

$$p_{\text{sym}}(\rho) = \rho^2 \frac{dE_{\text{sym}}(\rho)}{d\rho} \approx p_{\text{PNM}}(\rho) - p_{\text{SNM}}(\rho), \quad (16)$$

[the last equation is valid in case of the quadratic approximation Eq. (1)], which adds to the pressure of an isospin-symmetric system with $N = Z$. Its contribution is very important because it is related to the poorly known symmetry energy at large density, and plays a big role in the determination of the proton fraction, for instance, crucial for NS cooling simulations. More precisely, the pressure of metastable matter (including electrons) with asymmetry $\delta(\rho) = (\rho_n - \rho_e)/\rho$ is given by [83, 85, 86]

$$p_\beta(\rho) = p_{\text{SNM}}(\rho) + \delta^2 p_{\text{sym}}(\rho) + \frac{\delta(1-\delta)}{2} \rho E_{\text{sym}}(\rho). \quad (17)$$

For small electron fractions one has $\delta \approx 1$ and

$$p_{\text{sym}} \approx p_\beta - p_{\text{SNM}}. \quad (18)$$

This quantity is displayed in Fig. 3(d) using thick curves. The markers with error bars are the corresponding results of the analysis performed in Ref. [79], where a subtraction procedure has been proposed between the kaon data (white dots) and flow data (blue dots) for SNM, both displayed in panel (a), and the GW170817 event constraints shown in panel (c), assuming matter in beta-stable condition. We see that the symmetry pressure increases rapidly with the baryon density, as many microscopic EOSs predict, except at densities above $\rho \gtrsim 0.7 \text{ fm}^{-3}$, where most EOSs show a saturating behavior and thus a different trend with respect to the analysis of the (Flow) data. However, such high densities are never actually reached in HICs.

We also point out that the true symmetry pressure $p_{\text{sym}} \approx p_{\text{PNM}} - p_{\text{SNM}}$ [thin curves in Fig. 3(d)] can be substantially larger than the approximation Eq. (18), if one takes properly into account the EOS for PNM, which is significantly stiffer than the metastable EOS for most considered models, compare Figs. 3(b) and (c).

5.3 Correlations between neutron star and nuclear matter observables

In order to better understand the properties of nuclear matter, it would be very interesting to find correlations between GW170817 observations and microscopic constraints from nuclear measurements, as the ones just discussed. For this purpose, the limits derived for the tidal deformability could be very valuable.

We remind that the LIGO-Virgo collaborations performed a Bayesian analysis of the GW data, assuming

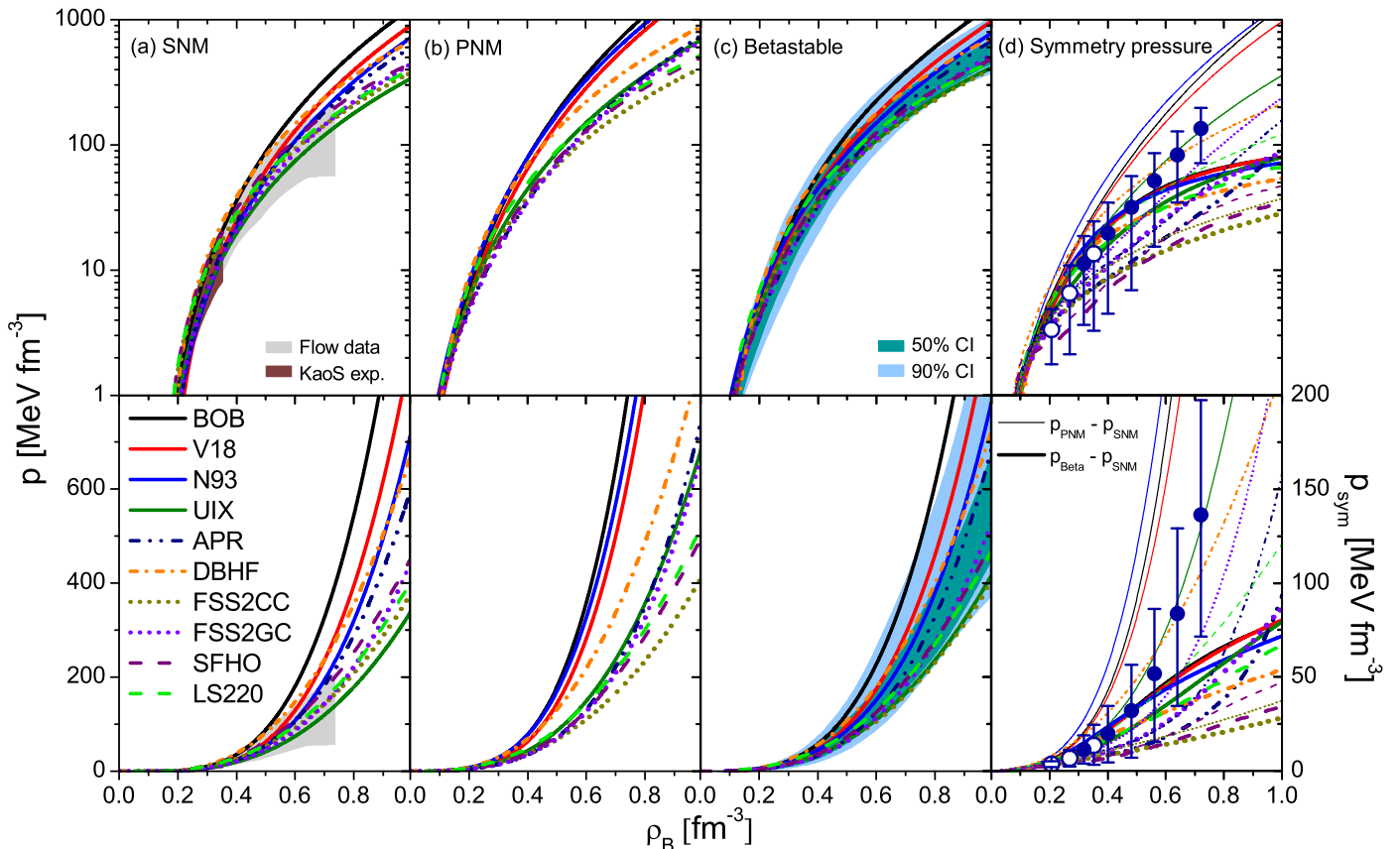


Fig. 3. Pressure vs. baryon density for the considered EOSs on a logarithmic (upper row) or linear (lower row) scale for (a) symmetric matter, (b) pure neutron matter, (c) beta-stable matter, and (d) the symmetry pressure. In (a) constraints derived from HIC data are reported as brown band (KaoS experiment) and grey band (Flow data). In (c) the GW170817 constraints [17] are reported. The markers in (d) are from the data analysis of Ref. [79]. The thick curves represent the compatible quantity $p_\beta - p_{\text{SNM}}$, whereas the actual symmetry pressure $p_{\text{PNM}} - p_{\text{SNM}}$ is shown by thin curves. See text for more details.

that each star may have different EOSs [16], thus deducing a bound on $\Lambda_{1.4} \leq 800$ for a $1.4 M_\odot$ NS. This bound rules out very stiff EOSs. Based on this result, the authors of Ref. [87] combined an EOS at low densities built with the chiral effective theory with perturbative QCD results at large densities, and constrained $R_{1.4} < 13.6$ km [88]. Similar results were obtained also in Refs. [88–92]. The improved analysis of the GW170817 merger event, performed using more realistic waveform models and assuming the same EOS for both stars, provided $70 < \Lambda_{1.4} < 580$ at 90% confidence level [17], which allowed to tighten the upper limit to $R_{1.4} < 12.9$ km in a recent analysis [93] in the framework of RMF models. The interpretation of the GW170817 event allowed to establish also *lower* limits on the NS radius, e.g., the measurement of the neutron skin thickness of ^{208}Pb by the PREX collaboration [94] gives $R_{1.4} > 12.55$ km [88], and this was confirmed by similar recent analyses [89, 90].

The source of GW170817 also released a short gamma-ray burst, GRB170817A, and a kilonova, AT2017gfo, generated by the mass ejected from the merger, and this was found to provide constraints on the EOS as well. In particular [21], a limit $\Lambda > 400$ on the average tidal deformability, Eq. (14), was deduced in order to eject mate-

rial heavier than $0.05 M_\odot$, as required by the high luminosity of AT2017gfo. This constraint could indicate that $R_{1.4} \gtrsim 12$ km, which was used in Refs. [89, 90, 92, 95] in order to constrain properties of nuclear matter. This lower limit has been recently loosened to $\Lambda \gtrsim 300$ [65], although in Ref. [67] it has been considered of limited significance.

We remind the reader that there are no precise simultaneous measurements of a NS mass and radius yet. To date, several different astrophysical measurements of NS radii have been attempted, and they still suffer of big uncertainties [8], especially related to the atmosphere composition. After the first inference of radii from the thermal emission from accreting NSs in quiescent low-mass X-ray binaries (QLMXBs) [76, 96], radii in the range 10.1–11.1 km have been deduced from new measurements with a larger sample of sources [97]. They are smaller than the lower limits derived from GW170817 observations. It has been suggested that this discrepancy (if confirmed) might be solved in the two-families or twin-star scenarios, in which small and big stars of the same mass could coexist as hadronic and quark matter stars [95, 98–100]. On the other hand, a different analysis was proposed in Ref. [70], where the radius estimates were inferred from photospheric radius expansion (PRE) bursts and thermal

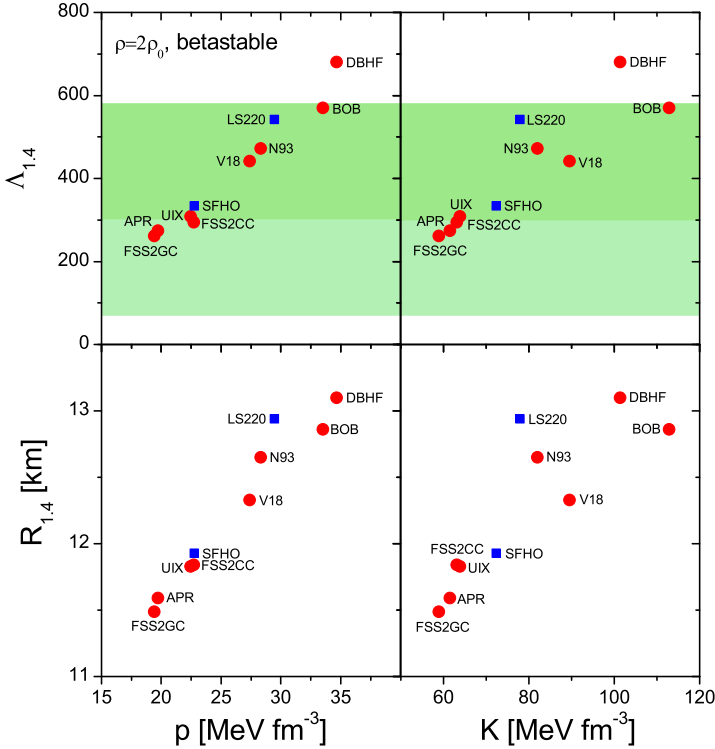


Fig. 4. Tidal deformability (upper panels) and radius (lower panels) of a $1.4 M_{\odot}$ NS vs. the pressure (left panels) and the incompressibility K (right panels) of betastable matter at twice the saturation density. The light and dark shaded bands in the upper row represent the limits derived in [17, 65], respectively.

emissions from QLMXBs and isolated NSs. In that case, typical radii, i.e., for 1.2 – $1.8 M_{\odot}$ stars, lie in the range 11.1 – 12.8 km, fully compatible with GW170817. These existing discrepancies could be overcome by the in-progress NASA Neutron Star Interior ExploreR (NICER) mission [12–14], which will hopefully provide in the near future radii measurements with uncertainties as small as 0.5 km.

We now turn to the discussion of our results. In Ref. [85] it was found that for a wide choice of nuclear EOSs the NS radius is strongly correlated with the pressure of betastable matter $p = \rho^2 dE_{\beta}/d\rho$ at a density $\rho \approx 2\rho_0$. According to the previous discussion this correlation is then also valid between $\Lambda_{1.4}$ and pressure. This is also confirmed for our set of EOSs as shown in Fig. 4 (left panels), whereas weaker correlations appear with the incompressibility $K = 9\rho^2 d^2E_{\beta}/d\rho^2$ under the same conditions, displayed in the right panels.

For completeness, we have calculated the correlation factors

$$r(x, y) = \frac{1}{n-1} \frac{\sum_x \sum_y (x - \bar{x})(y - \bar{y})}{s_x s_y}, \quad (19)$$

where n is the number of data pairs, \bar{x} and \bar{y} are the sample means of all the x and y values, respectively; and s_x and s_y are their standard deviations. In our case the

results are

$$r(p, \Lambda_{1.4}) = 0.982, \quad r(p, R_{1.4}) = 0.971, \quad (20)$$

$$r(K, \Lambda_{1.4}) = 0.885, \quad r(K, R_{1.4}) = 0.846, \quad (21)$$

which confirm the above statements, i.e., stronger (weaker) correlations among pressure p , $\Lambda_{1.4}$, and $R_{1.4}$ (K , $\Lambda_{1.4}$, and $R_{1.4}$).

The green bands displayed in the upper panels represent the limits on $\Lambda_{1.4}$ derived in [17, 65], in particular the lower limits, i.e., $\Lambda_{1.4} = 190^{+390}_{-120}$ [17] (light green) and $\Lambda_{1.4} > 300$ [65, 66] (dark green), are important for the determination of the radius, which corresponds to $R_{1.4} = 11.9^{+1.4}_{-1.4}$ km in the former case, and $R_{1.4} = 12.2^{+1.0}_{-0.8} \pm 0.2$ km in the latter one. For completeness, we have checked whether this correlation applies also to NS masses different from $1.4 M_{\odot}$, but it becomes slightly weaker with increasing NS masses. Thus the determination of the tidal deformability or the NS radius could put constraints on the pressure and the symmetry pressure at twice the saturation density [64, 85]. The current limits exclude only the DBHF EOS due to its too high $\Lambda_{1.4}$ value.

Following the same philosophy, we have tried to find correlations between NS observables and properties of SNM around saturation density. Results are displayed in Fig. 5 (the green bands display the same conditions as in Fig. 4), where the tidal deformability of a $1.4 M_{\odot}$ NS is reported as a function of the symmetry energy S_0 (left panel), its slope L (middle panel), and the incompressibility K_0 (right panel), all taken at saturation density. Apparently no evident correlations between the tidal deformability and S_0 and K_0 do exist, whereas some degree of correlation is found with L , as confirmed by the corresponding correlation factors

$$r([S_0, K_0, L], \Lambda_{1.4}) = [0.128, 0.300, 0.808]. \quad (22)$$

Similar results were found also in Refs. [54, 92, 101, 102], with several EOSs based on the RMF model and the Skyrme-Hartree-Fock approach.

6 Summary

We conclude that among the BHF models analyzed here, the V18 and N93 could be good candidates for a realistic description of the nuclear EOS up to very high density. They fulfill nearly all current experimental and observational constraints discussed in this article, in particular the novel constraints on the tidal deformability imposed by GW170817. We would like to emphasize that these are not phenomenological EOSs, but they have been constructed in a microscopic way from nuclear two-body potentials and compatible three-body forces. The last issue imposed in fact strong conditions on their construction, due to which reason a perfect reproduction of all current constraints is not achieved, but was also not attempted. We stress in particular that the predicted maximum mass values $\approx 2.3 M_{\odot}$ could be close to the ‘true’ maximum mass

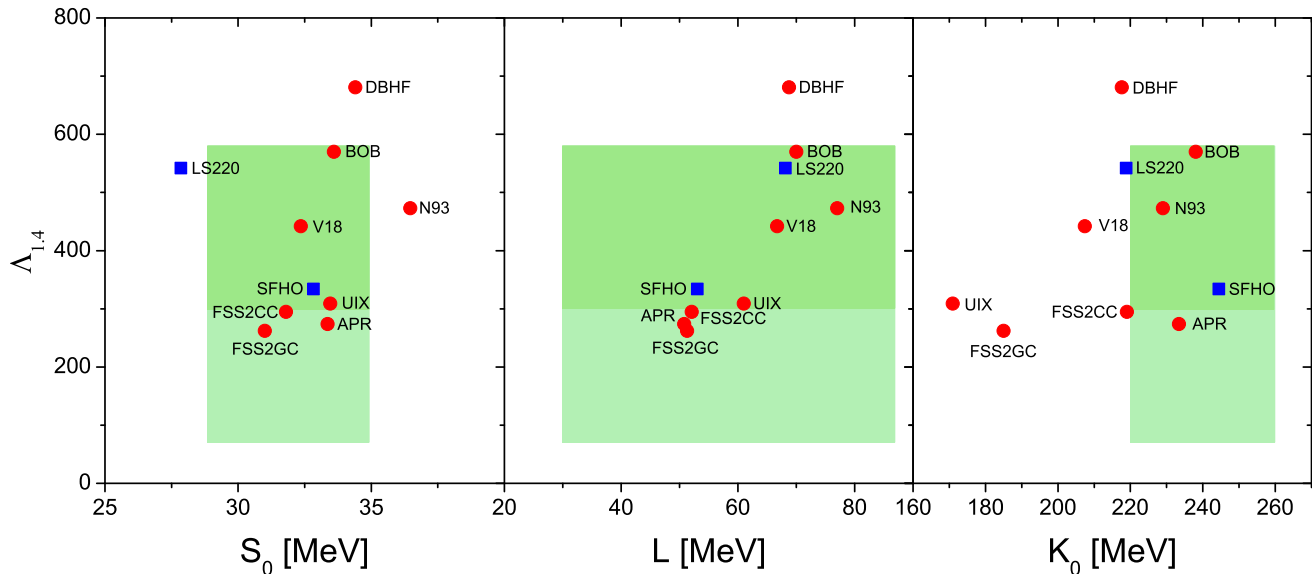


Fig. 5. The tidal deformability of a $1.4 M_{\odot}$ NS as a function of the symmetry energy (left panel), its derivative L (middle panel), and the incompressibility K_0 at saturation density ρ_0 for all the considered EOSs. The shaded areas represent the limits listed in Table 1.

conjectured from the GW170817 event. The two models predict then $R_{1.4} = 12.3, 12.7$ km, respectively.

The new astrophysical constraints on maximum mass and tidal deformability exclude several models with too small maximum mass and the DBHF EOS with a too large deformability. Tightening the lower limit on $\Lambda_{1.4}$ could potentially exclude several other EOSs.

For all examined EOSs we also confirmed the correlation between the radius or deformability of a $1.4 M_{\odot}$ NS and the pressure of metastable matter at about twice normal density. Weaker correlations were found with the compressibility of metastable matter at that density. On the other hand, we did not find any clear correlations between NS deformability and properties of symmetric matter at normal density.

Acknowledgments

This work is sponsored by the National Natural Science Foundation of China under Grant Nos. 11075037, 11975077 and the China Scholarship Council, File Nos. 201706410092 and 2018 06100066. Partial support comes also from “PHAROS” COST Action CA16214.

Appendix: Parametrizations of the BHF EOSs

For convenience we provide here simple parametrizations of our numerical results for the different EOSs, namely analytical fits of the energy per nucleon E for SNM and PNM. We find that in both cases the following functional forms constitute excellent representations of the numerical values

$$E(\rho) = a\rho + b\rho^c + d, \quad (23)$$

Table 2. Parameters of the fit for the energy per nucleon E , Eq. (23), for symmetric nuclear matter (SNM) and pure neutron matter (PNM) in two different density domains and for the different EOSs used.

EOS		$\rho = (0.08-1) \text{ fm}^{-3}$				$\rho = (0.14-0.21) \text{ fm}^{-3}$			
		a	b	c	d	a	b	c	d
BOB	SNM	-65	498	2.67	-9	-189	446	1.83	-0.83
	PNM	57	856	2.91	4	15	584	2.37	7.11
V18	SNM	-60	369	2.66	-8	-82	487	2.58	-4.96
	PNM	37	667	2.78	6	38	578	2.67	5.88
N93	SNM	-42	298	2.61	-12	-62	803	3.20	-8.18
	PNM	67	743	2.71	4	42	471	2.48	5.47
UIX	SNM	-174	323	1.61	-4	-46	926	3.38	-9.29
	PNM	24	326	2.09	6	31	294	2.10	6.25

where E and ρ are given in MeV and fm^{-3} , respectively. The parameters of the fits are listed in Table 2 for the different EOSs we are using. We provide two sets of parametrizations, i.e., a first set to be used for NS structure calculations in the density range $(0.08-1) \text{ fm}^{-3}$, and a second set for the range $(0.14-0.21) \text{ fm}^{-3}$, more appropriate for a precise determination of the saturation properties. The rms deviations of fits and data are better than 1 MeV / 0.02 MeV for the two cases and for all EOSs.

For asymmetric nuclear matter, it turns out that the dependence on proton fraction $x_p = (1 - \delta)/2$ can be very well approximated by a parabolic law as assumed in Eq. (1) [28, 103],

$$E(\rho, \delta) \approx E_{\text{SNM}}(\rho) + \delta^2 [E_{\text{PNM}}(\rho) - E_{\text{SNM}}(\rho)]. \quad (24)$$

Therefore, for the treatment of the asymmetric and beta-stable case, it is only necessary to provide parametrizations for SNM and PNM.

References

1. J.M. Lattimer, M. Prakash, *Phys. Rep.* **621**, 127 (2016)
2. G.F. Burgio, A.F. Fantina, *Astrophys. Space Sci.Libr.* **457**, 255 (2018)
3. J.M. Lattimer, *Ann. Rev. Nucl. Sci.* **62**, 485 (2012)
4. P.B. Demorest, T. Pennucci, S.M. Ransom, M.S. Roberts, J.W. Hessels, *Nature* **467**, 1081 (2010)
5. E. Fonseca et al., *Astrophys. J.* **832**, 167 (2016)
6. J. Antoniadis et al., *Science* **340**, 6131 (2013)
7. H.T. Cromartie et al., *Nature Astronomy* (2019), 1904.06759
8. F. Özel, P. Freire, *Ann. Rev. Astron. Astrophys.* **54**, 401 (2016)
9. S. Guillot, M. Servillat, N.A. Webb, R.E. Rutledge, *Astrophys. J.* **772**, 7 (2013)
10. J.M. Lattimer, A.W. Steiner, *Astrophys. J.* **784**, 123 (2014)
11. M.G. Alford, G.F. Burgio, S. Han, G. Taranto, D. Zappalà, *Phys. Rev. D* **92**, 083002 (2015)
12. <https://www.nasa.gov/nicer/>
13. Arzumanyan, Z. et al., *Proceedings of SPIE* **9144**, 914420 (2014)
14. S. Bogdanov, *AAS/High Energy Astrophysics Division* **15**, 105.05 (2016)
15. A.L. Watts et al., *Science China Physics, Mechanics, and Astronomy* **62**, 29503 (2019)
16. B. Abbott et al., *Phys. Rev. Lett.* **119**, 161101 (2017)
17. B.P. Abbott et al., *Phys. Rev. Lett.* **121**, 161101 (2018)
18. B.P. Abbott et al., *Phys. Rev. X* **9**, 011001 (2019)
19. J.B. Hartle, *Astrophys. J.* **150**, 1005 (1967)
20. E.E. Flanagan, T. Hinderer, *Phys. Rev. D* **77**, 021502 (2008)
21. D. Radice, A. Perego, F. Zappa, S. Bernuzzi, *Astrophys. J.* **852**, L29 (2018)
22. J.P. Jeukenne, A. Lejeune, C. Mahaux, *Phys. Rep.* **25**, 83 (1976)
23. M. Baldo, *International Review of Nuclear Physics (World Scientific, Singapore)* **8** (1999)
24. J.J. Lu, Z.H. Li, C.Y. Chen, M. Baldo, H.J. Schulze, *Phys. Rev. C* **96**, 044309 (2017)
25. J.J. Lu, Z.H. Li, C.Y. Chen, M. Baldo, H.J. Schulze, *Phys. Rev. C* **98**, 064322 (2018)
26. Z.H. Li, H.J. Schulze, *Phys. Rev. C* **94**, 024322 (2016)
27. P. Grangé, A. Lejeune, M. Martzoff, J.F. Mathiot, *Phys. Rev. C* **40**, 1040 (1989)
28. M. Baldo, I. Bombaci, G.F. Burgio, *Astron. Astrophys.* **328**, 274 (1997)
29. W. Zuo, A. Lejeune, U. Lombardo, J.F. Mathiot, *Eur. Phys. J. A* **14**, 469 (2002)
30. Z.H. Li, U. Lombardo, H.J. Schulze, W. Zuo, *Phys. Rev. C* **77**, 034316 (2008)
31. Z.H. Li, H.J. Schulze, *Phys. Rev. C* **78**, 028801 (2008)
32. R. Machleidt, K. Holinde, C. Elster, *Phys. Rep.* **149**, 1 (1987)
33. R. Machleidt, *Adv. Nucl. Phys.* **19**, 189 (1989)
34. M.M. Nagels, T.A. Rijken, J.J. de Swart, *Phys. Rev. D* **17**, 768 (1978)
35. V.G.J. Stoks, R.A.M. Klomp, C.P.F. Terheggen, J.J. de Swart, *Phys. Rev. C* **49**, 2950 (1994)
36. R.B. Wiringa, V.G.J. Stoks, R. Schiavilla, *Phys. Rev. C* **51**, 38 (1995)
37. J. Margueron, R. Hoffmann Casali, F. Gulminelli, *Phys. Rev. C* **97**, 025805 (2018)
38. S. Shlomo, V.M. Kolomietz, G. Colò, *EPJA* **30**, 23 (2006)
39. J. Piekarewicz, *Journal of Physics G Nuclear Physics* **37**, 064038 (2010)
40. B.A. Li, X. Han, *Phys. Lett. B* **727**, 276 (2013)
41. M. Oertel, M. Hempel, T. Klähn, S. Typel, *Reviews of Modern Physics* **89**, 015007 (2017)
42. M. Baldo, K. Fukukawa, *Phys. Rev. Lett.* **113**, 242501 (2014)
43. K. Fukukawa, M. Baldo, G.F. Burgio, L. Lo Monaco, H.J. Schulze, *Phys. Rev. C* **92**, 065802 (2015)
44. T. Gross-Boelting, C. Fuchs, A. Faessler, *Nucl. Phys. A* **648**, 105 (1999)
45. A. Akmal, V.R. Pandharipande, D.G. Ravenhall, *Phys. Rev. C* **58**, 1804 (1998)
46. J.M. Lattimer, F.D. Swesty, *Nucl. Phys. A* **535**, 331 (1991)
47. A.W. Steiner, M. Hempel, T. Fischer, *Astrophys. J.* **774**, 17 (2013)
48. J.W. Negele, D. Vautherin, *Nucl. Phys. A* **207**, 298 (1973)
49. G. Baym, C. Pethick, P. Sutherland, *Astrophys. J.* **170**, 299 (1971)
50. R.P. Feynman, N. Metropolis, E. Teller, *Phys. Rev.* **75**, 1561 (1949)
51. G.F. Burgio, H.J. Schulze, *Astron. Astrophys.* **518**, A17 (2010)
52. M. Baldo, G.F. Burgio, M. Centelles, B.K. Sharma, X. Viñas, *Physics of Atomic Nuclei* **77**, 1157 (2014)
53. M. Fortin, C. Providência, A.R. Raduta, F. Gulminelli, J.L. Zdunik, P. Haensel, M. Bejger, *Phys. Rev. C* **94**, 035804 (2016)
54. C.Y. Tsang, M.B. Tsang, P. Danielewicz, F.J. Fattoyev, W.G. Lynch, *Physics Letters B* **796**, 1 (2019), 1905.02601
55. I. Tews, J.M. Lattimer, A. Ohnishi, E.E. Kolomeitsev, *Astrophys. J.* **848**, 105 (2017)
56. N.B. Zhang, B.J. Cai, B.A. Li, W.G. Newton, J. Xu, *Nucl. Sci. Tech.* **28**, 181 (2017)
57. M. Shibata, S. Fujibayashi, K. Hotokezaka, K. Kiuchi, K. Kyutoku, Y. Sekiguchi, M. Tanaka, *Phys. Rev. D* **96**, 123012 (2017)
58. B. Margalit, B.D. Metzger, *Astrophys. J.* **850**, L19 (2017)
59. L. Rezzolla, E.R. Most, L.R. Weih, *Astrophys. J.* **852**, L25 (2018)
60. M. Shibata, E. Zhou, K. Kiuchi, S. Fujibayashi, *Phys. Rev. D* **100**, 023015 (2019)

61. T. Hinderer, *Astrophys. J.* **677**, 1216 (2008)
62. T. Hinderer, *Astrophys. J.* **697**, 964 (2009)
63. T. Hinderer, B.D. Lackey, R.N. Lang, J.S. Read, *Phys. Rev. D* **81**, 123016 (2010)
64. J.M. Lattimer, M. Prakash, *Phys. Rep.* **442**, 109 (2007)
65. D. Radice, L. Dai, *EPJA* **55**, 50 (2019)
66. M.W. Coughlin, T. Dietrich, B. Margalit, B.D. Metzger, *Mon. Not. R. Astron. Soc.* p. L131 (2019)
67. K. Kiuchi, K. Kyutoku, M. Shibata, K. Taniguchi, *Astrophys. J. Lett.* **876**, L31 (2019)
68. M.B. Tsang et al., *Phys. Rev. C* **86**, 015803 (2012)
69. J.M. Lattimer, Y. Lim, *Astrophys. J.* **771**, 51 (2013)
70. J.M. Lattimer, A.W. Steiner, *EPJA* **50**, 40 (2014)
71. M.B. Tsang, Y. Zhang, P. Danielewicz, M. Famiano, Z. Li, W.G. Lynch, A.W. Steiner, *Phys. Rev. Lett.* **102**, 122701 (2009)
72. X. Roca-Maza, X. Viñas, M. Centelles, B.K. Agrawal, G. Colò, N. Paar, J. Piekarewicz, D. Vretnar, *Phys. Rev. C* **92**, 064304 (2015)
73. L.W. Chen, C.M. Ko, B.A. Li, J. Xu, *Phys. Rev. C* **82**, 024321 (2010)
74. P. Möller, W.D. Myers, H. Sagawa, S. Yoshida, *Phys. Rev. Lett.* **108**, 052501 (2012)
75. P. Danielewicz, J. Lee, *Nucl. Phys. A* **922**, 1 (2014)
76. A.W. Steiner, J.M. Lattimer, E.F. Brown, *Astrophys. J. Lett.* **765**, L5 (2013)
77. P. Russotto et al., *Phys. Rev. C* **94**, 034608 (2016)
78. P. Russotto et al., *Phys. Lett. B* **697**, 471 (2011)
79. C.Y. Tsang, M.B. Tsang, P. Danielewicz, W.G. Lynch, F.J. Fattoyev, arXiv (2019), 1901.07673
80. D. Miśkowiec, *Phys. Rev. Lett.* **72**, 3650 (1994)
81. P. Danielewicz, R. Lacey, W.G. Lynch, *Science* **298**, 1592 (2002)
82. J.L. Ritman et al., *Z. Phys. A* **352**, 355 (1995)
83. N.B. Zhang, B.A. Li, *Astrophys. J.* **879**, 99 (2019)
84. C.Y. Tsang, M.B. Tsang, P. Danielewicz, W.G. Lynch, F.J. Fattoyev, arXiv (2018), 1807.06571
85. J.M. Lattimer, M. Prakash, *Phys. Rep.* **333**, 121 (2000)
86. N.B. Zhang, B.A. Li, *European Physical Journal A* **55**, 39 (2019)
87. E. Annala, T. Gorda, A. Kurkela, A. Vuorinen, *Phys. Rev. Lett.* **120**, 172703 (2018)
88. F.J. Fattoyev, J. Piekarewicz, C.J. Horowitz, *Phys. Rev. Lett.* **120**, 172702 (2018)
89. E.R. Most, L.R. Weih, L. Rezzolla, J. Schaffner-Bielich, *Phys. Rev. Lett.* **120**, 261103 (2018)
90. Y. Lim, J.W. Holt, *Phys. Rev. Lett.* **121**, 062701 (2018)
91. C. Raithel, F. Özel, D. Psaltis, *Astrophys. J.* **857**, L23 (2018)
92. T. Malik, N. Alam, M. Fortin, C. Providência, B.K. Agrawal, T.K. Jha, B. Kumar, S.K. Patra, *Phys. Rev. C* **98**, 035804 (2018)
93. R. Nandi, P. Char, S. Pal, *Phys. Rev. C* **99**, 052802 (2019)
94. S. Abrahamyan et al., *Phys. Rev. Lett.* **108**, 112502 (2012)
95. G.F. Burgio, A. Drago, G. Pagliara, H.J. Schulze, J.B. Wei, *Astrophys. J.* **860**, 139 (2018)
96. F. Özel, G. Baym, T. Güver, *Phys. Rev. D* **82**, 101301 (2010)
97. F. Özel, D. Psaltis, T. Güver, G. Baym, C. Heinke, S. Guillot, *Astroph. J.* **820**, 28 (2016)
98. A. Drago, G. Pagliara, *Astrophys. J.* **852**, L32 (2018)
99. G. Wiktorowicz, A. Drago, G. Pagliara, S.B. Popov, *Astrophys. J.* **846**, 163 (2017)
100. V. Paschalidis, K. Yagi, D. Alvarez-Castillo, D.B. Blaschke, A. Sedrakian, *Phys. Rev. D* **97**, 084038 (2018)
101. F.J. Fattoyev, J. Carvajal, W.G. Newton, B.A. Li, *Phys. Rev. C* **87**, 015806 (2013)
102. L. Perot, N. Chamel, A. Sourie, *Phys. Rev. C* **100**, 035801 (2019)
103. I. Bombaci, U. Lombardo, *Phys. Rev. C* **44**, 1892 (1991)